The Astrophysical Journal, 953:100 (8pp), 2023 August 10 https://doi.org/10.3847/1538-4357/ace344

The Nature of γ-Ray Emission from HESS J1912+101

Yuan Li[1,2,3], Siming Liu[1], and Yu He[1]
[1] School of Physical Science and Technology, Southwest Jiaotong University, Chengdu 610031, People's Republic of China; liusm@swjtu.edu.cn, heyujy@swjtu.edu.cn
[2] Tsung-Dao Lee Institute, Shanghai Jiao Tong University, Shanghai 200240, People's Republic of China
[3] School of Physics and Astronomy, Shanghai Jiao Tong University, Shanghai 200240, People's Republic of China
Received 2023 May 2; revised 2023 June 24; accepted 2023 June 29; published 2023 August 8

Abstract

Since the discovery of HESS J1912+101 at teraelectronvolt energies, its nature has been extensively studied. Due to the absence of X-ray and radio counterparts, whether its γ-ray emission is produced by relativistic electrons or ions is still a matter of debate. We reanalyze its megaelectronvolt to gigaelectronvolt γ-ray emission using 14 yr of Pass 8 data of the Fermi-LAT, and find that the gigaelectronvolt γ-ray emission is more extended than the teraelectronvolt shell detected by H. E. S. S. and flux above 10 GeV from the northern half is much higher than that from the southern half, where there is evident interaction between shocks and molecular clouds. As a consequence, the gigaelectronvolt spectrum of the northern half (with an index of 2.19 ± 0.12) is much harder than that in the south (with an index of 2.72 ± 0.08), and the overall gigaelectronvolt spectrum shows a concave shape, which is distinct from most γ-ray supernova remnants (SNRs). In combination with the teraelectronvolt spectrum, the overall γ-ray spectrum can be fitted with a broken power-law model for trapped ions and a low energy component due to escaping ions. The diffusion coefficient for escaping ions however needs to be proportional to the energy, implying that the low energy component may also be attributed to ions accelerated via recent shock–cloud interactions. A hadronic origin for the γ-ray emission is therefore favored and the overall emission properties are consistent with ion acceleration by SNR shocks. On the other hand, it is still undeniable that stellar cluster or PWN may have some contribution in some parts of this extended source.

Unified Astronomy Thesaurus concepts: Supernova remnants (1667); Molecular clouds (1072); High energy astrophysics (739)

1. Introduction

Supernova remnants (SNRs) are generally regarded as the most likely acceleration sites of Galactic cosmic rays (CRs) below energies of the knee (Ginzburg & Syrovatskii 1964; Hillas 2005). SNRs interacting with dense molecular clouds (MoCs) are expected to be bright in the γ-ray band. Effectively, the γ-ray emissions from such systems have been detected by the Fermi Large Area Telescope (Fermi-LAT), including γ-Cygni (Acciari et al. 2023), IC 443 (Abdo et al. 2010; Ackermann et al. 2013), W44 (Uchiyama et al. 2012; Peron et al. 2020), W28 (Aharonian et al. 2008a; Li & Chen 2010; Hanabata et al. 2014) and W51C (Abdo et al. 2009). The intense gigaelectronvolt γ-ray emissions from these SNRs are commonly considered to be from the decay of neutral pions generated in inelastic collisions between accelerated protons and the dense gas in MoCs. Notably, the γ-ray spectra of W51C, W44, and IC 443 have shown spectral features of π^0 decay, which are considered to be the most definitive proof for the presence of relativistic nuclei acceleration in SNRs.

Diffusive shock acceleration (DSA) operating at expanding shock waves of SNRs is widely regarded as the mechanism converting the kinetic energy released by supernova explosions into the energy of CRs (Malkov & Drury 2001). For the DSA mechanism, CRs being accelerated at the shock of SNR could be scattered by self-generated magnetic turbulence. And the highest-energy CRs near the shock precursor are prone to lack self-generated turbulence, which portends to escape from the SNR. The DSA mechanism generally portends that a substantial fraction of the shock energy is carried away by escaping CRs. In the presence of molecular clouds surrounding the SNR, these clouds could be illuminated by the escaping CRs producing γ-ray emission through the *pp* interactions. And γ-ray flux depends on the amount of nuclear CRs released and the diffusion coefficient in the interstellar medium (ISM; Aharonian & Atoyan 1996; Aharonian et al. 2004; Rodriguez Marrero et al. 2008; Gabici et al. 2009). For the γ-ray sources associated with clouds illuminated by escaped CRs from nearby SNRs, the measurement of the γ-ray spectrum can help to study the diffusion process and limit the energy dependence of the diffusion coefficient in the interstellar medium (Aharonian & Atoyan 1996; Ohira et al. 2011).

HESS J1912+101 was first discovered in 2008 by the H. E. S. S. Collaboration (Aharonian et al. 2008b), which is suggested to be a possible SNR due to the shell-like structure of the teraelectronvolt emission (Abdalla et al. 2018) shown as Figure 1. Its radio counterpart will not be able to be detected until polarization measurement (Reich & Sun 2019) becomes available, indicating the existence of its surrounding powerful large-scale magnetic field. Observations of dense gas in the region of HESS J1912+101 show that it is associated with an old SNR whose age is 70–200 kyr (Su et al. 2017), which concurs with the characteristic age of 170 kyr for pulsar PSR J1913+101 (Morris et al. 2002) inside this SNR. However, the suggested size of the teraelectronvolt source 2HWC J1912 +099 measured by Abeysekara et al. (2017) and 3HWC J1912 +103 (Albert et al. 2020) are distinct from the H. E. S. S. source, which can be attributed to the discrepancy in

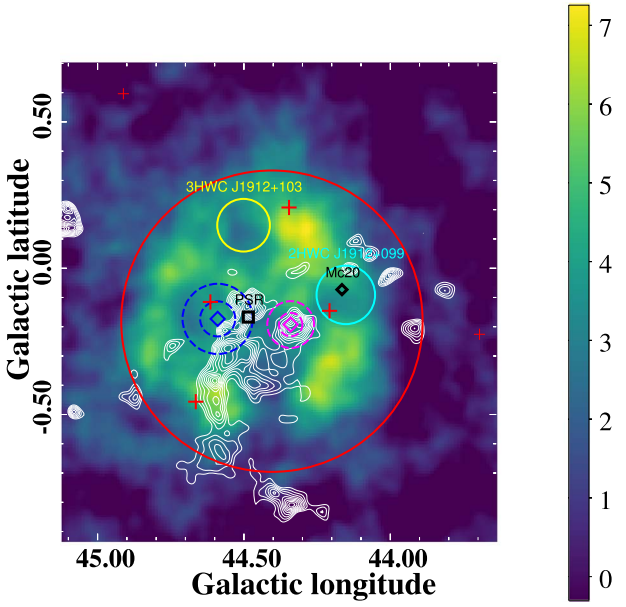

Figure 1. Teraelectronvolt γ-ray emission map of HESS J1912+101 in Galactic coordinates (Abdalla et al. 2018). The cyan and yellow circles show the central position with 1σ statistical uncertainty measured by 2HWC J1912 +099 (Abeysekara et al. 2017) and 3HWC J1912+103 (Albert et al. 2020), respectively. The red crosses indicate 4FGL sources in this region. The black square represents the location of PSR J1913+1011 (Morris et al. 2002). The black diamond shows the location of Mc20 (Messineo et al. 2009; Sun et al. 2022). The white contours show the integrated ^{13}CO ($J = 1$-0) emission intensity in this work. The red circle shows the 68% containment radius of the best-fit uniform disk model in this work. Blue and magenta diamonds with dashed circles correspond to two γ-ray sources with 1σ and 2σ error radii revealed by Fermi-LAT in this work. See the text and Figure 2 for details.

sensitivities and fields of view between these two telescopes. Additionally, Observations from Chandra data show that no credible X-ray counterparts have been found (Chang et al. 2008). The origin of γ-ray emission from this source remains obscure. Recent γ-ray analysis results by Sun et al. (2022) suggest part of the gigaelectronvolt emission comes from the young massive star cluster Mc20, and Zeng et al. (2021) show that the old age of the SNR favors a hadronic origin for the teraelectronvolt emission. On the other hand, Zhang et al. (2020) show that a leptonic origin associated with the pulsar cannot be ruled out.

In this work, we will report the analysis results of the gigaelectronvolt γ-ray emission toward HESS J1912+101 using more than 14 yr Fermi-LAT data in the energy range of 100 MeV to 1 TeV, which is shown in Section 2. Meanwhile, the ^{13}CO($J = 1$–0) observational results of molecular clouds in this region will be presented in Section 3 to reveal the origin of the γ-ray emission. In Section 4, we discuss the interpretation of the gigaelectronvolt γ-ray emission. Lastly, we provide our conclusions in Section 5.

2. Fermi-LAT Data Analysis

Fermi-LAT is sensitive to γ-rays with energies from 20 MeV to more than 300 GeV, and it has continuously monitored the sky since 2008 (Atwood et al. 2009). The Pass 8 data from 2008 August 4 to 2022 August 4 are taken to study the gigaelectronvolt emission around the HESS J1912+101 region. The event class "P8R3_SOURCE" (evclass = 128) and event type FRONT + BACK (evtype = 3) are used, with the standard data quality selection criteria (`DATA_QUAL` > 0)&& (`LAT_CONFIG==1`). Taking into account a better point-spread function (PSF) in the higher energy band as well as sufficient statistic events for the analysis, only events above 2 GeV are selected to determine the best spatial template, where the PSF is sharp enough to disentangle multiple components. Details of the spectral analysis for each component starting from the lower energy band will be shown in the following energy spectrum part. To minimize the contamination from the Earth's limb, the maximum zenith angle is set to be 90°. In this work, the publicly available software Fermitools (v.1.2.23) is used to perform the data analysis. The data within a $10° \times 10°$ region of interest (ROI) centered at the position of HESS J1912 +101 are considered for the binned maximum likelihood analysis (Mattox et al. 1996), and the instrument response function "P8R3_SOURCE_V3" is used. The diffuse Galactic interstellar emission (IEM, `gll_iem_v07.fits`), the isotropic emission (`iso_P8R3_SOURCE_V3_v1.txt`), and all sources listed in the fourth Fermi-LAT catalog (Abdollahi et al. 2020) are included in the background model. All sources within 5° from the center of the ROI are set free, together with the parameters of IEM and isotropic emission. The maximum likelihood test statistic (TS) is used to estimate the significance of the γ-ray sources, which is defined as $\mathrm{TS} = 2(\ln \mathcal{L}_1 - \ln \mathcal{L}_0)$, where $\mathcal{L}_1$ and $\mathcal{L}_0$ are maximum likelihood values for the background with target source and without target source (null hypothesis).

2.1. Morphological Analysis

We first study the energy dependence of the morphology of the γ-ray emission in the vicinity of HESS J1912+101. The TS map is generated by only considering background fitting but not including four 4FGL sources (4FGL J1914.7+1012, 4FGL J1911.7+1014, 4FGL J1912.7+0957, and 4FGL J1913.3 +1019), the γ-ray emission in the 2–1000, 2–10, and 10–1000 GeV ranges are shown in the top, left (bottom), right (bottom) panels of Figure 2. Obviously, the γ-ray emission has shifted as the energy band changes, similar to the TS map in the 2–1000 GeV range, the γ-ray emission in 2–10 GeV shows two regions of excess: one is located in the northern part and the other is in the southern part. In the 10–1000 GeV range, the γ-ray emission mainly distributed at the position of 4FGL J1913.3+1019 is seen. In order to select the best spatial template of the γ-ray emission in this region, we first added a single pointlike source into the model (Model 1), and optimized its localization using the *gtfindsrc* command, after subtracting the contribution from this source, strong γ-ray emission is still available; thus, we added another pointlike source into the model (Model 2) and refitted their locations with *gtfindsrc*, and the derived best-fit positions are R.A. = 288.°394, decl. = 10.°281, $r_{68_{\mathrm{NorthPoint}}} = 0.°06$ and R.A. = 288.°293, decl. = 10.°051, $r_{68_{\mathrm{SouthPoint}}} = 0.°04$ for the northern and southern γ-ray excess, respectively. After that, the Fermipy tool (Wood et al. 2017) is adopted to quantitatively evaluate the extension and location of the single uniform disk (Model 3) and 2D Gaussian (Model 4) templates, and the best-fit results are R.A. = 288.°310, decl.= 10.°112, $r_{68_{\mathrm{Disk}}} = 0.°515$ and R.A. = 288.°295, decl.= 10.°114, $r_{68_{\mathrm{Gaussian}}} = 0.°697$, respectively. In addition, we tested an extended source plus a point-source scenario (Model 5 and Model 6), while compared to a single extended template scenario (Model 3 and Model 4), the TS values and likelihood values did not improve significantly whether we localized with *gtfindsrc* command or fixed the

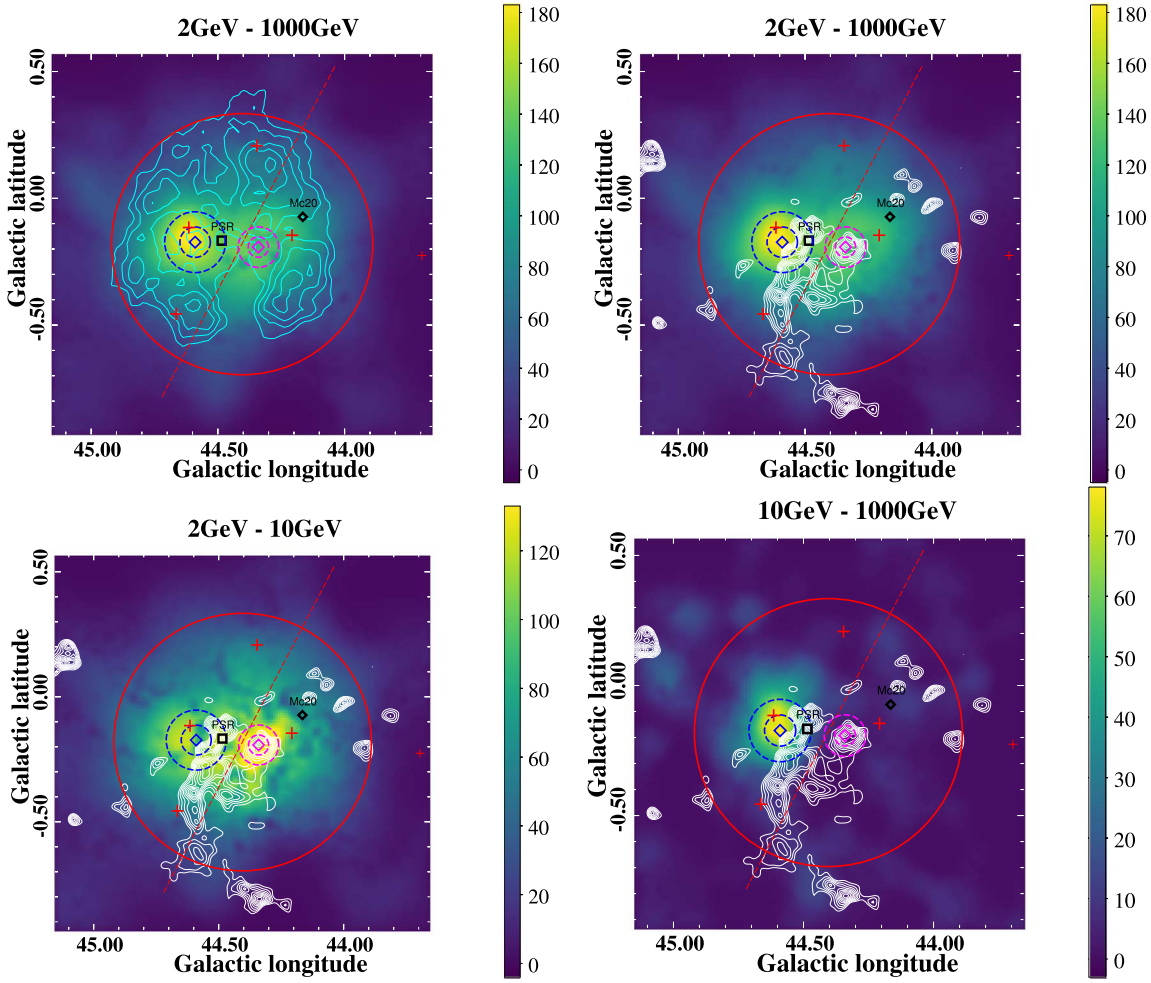

Figure 2. 1.°5 × 1.°5 TS maps in the vicinity of HESS J1912+101 observed with Fermi-LAT. All maps are given with square bins of 0.01°. The energy ranges are 2–1000 GeV (top panel), 2–10 GeV (bottom left panel), and 10–1000 GeV (bottom right panel), respectively. The red circle shows the best-fit position with r_{68} of the uniform disk in this work. The dashed line separates this circle into SrcN to the left and SrcS to the right. The red crosses show 4FGL sources. The blue and magenta diamond mark the position of two γ-ray sources derived from Model 2. The dashed circles represent the 1σ and 2σ error radii, respectively. The cyan contours show the teraelectronvolt γ-ray emission map, which is the same as that in Figure 1. The white contours represent the ^{13}CO($J = 1$–0) intensity integrated over a velocity range between 58.5 and 62.0 km s^{-1} the same as in Su et al. (2017).

point source at the PSR position. To further verify the energy-dependent morphology as indicated in Figure 2, we divide the uniform disk template into two half-disks (Model 7) along the western/eastern line in celestial coordinates, (hereafter, we refer to these as SrcN and SrcS, respectively). Thereafter, we also test the H. E. S. S. significance map (Model 8) as the template to show the spatial correlation between the gigaelectronvolt morphology and the teraelectronvolt shell. The extension σ represents the radius containing 68% of the intensity, and we define it as the source size. The TS_{ext} is defined as $TS_{ext} = 2(\ln \mathcal{L}_{ext} - \ln \mathcal{L}_{ps})$, where $\mathcal{L}_{ext}$ is the maximum likelihood value for the extended model and $\mathcal{L}_{ps}$ is the maximum likelihood value for the pointlike model, and the threshold required to regard a LAT source as extended is $TS_{ext} > 16$ (Lande et al. 2012). In the uniform disk template, TS_{ext} is calculated as 133, which rejects the pointlike source hypothesis at 11.5σ. The two-dimensional Gaussian template showed a similar result, $TS_{ext} = 139$ (corresponding to 11.8σ) demonstrating the source is significantly extended with respect to the LAT PSF. The two half-disk template provides a marginal improvement $\sim 2.8\sigma$. In addition, we use the Akaike information criterion (AIC; Akaike 1974) to assess the difference between these models, which is defined as $AIC = 2k - 2\ln \mathcal{L}$, where k is the number of degrees of freedom of the model and $\mathcal{L}$ is the likelihood value, and the model with a minimum AIC value is preferred. As shown in Table 1, the two half-disk case (Model 7) is adopted to perform further spectral analysis.

2.2. Energy Spectrum

After the morphology was fixed, we derived the γ-ray spectral of the whole disk (Model 3), and SrcN and SrcS (Model 7). Under the power-law assumption, the spectral indices show a significant difference in the 2–1000 GeV energy band, and the results are summarized in Table 2. Then, we tested the simple power-law (PL) and broken power-law (BPL) spectra using data ranging from 100 MeV to 1 TeV. As shown in Table 3, compared with the single PL model, the BPL model has an obvious improvement in the fitting. And the TS_{curve} value defined as $TS_{curve} = 2(\ln \mathcal{L}_{BPL} - \ln \mathcal{L}_{PL})$(Abdollahi et al. 2020) is calculated to be 204.69, which corresponds to a significance level of $\sim 14.3\sigma$. Therefore, we conclude that the spectrum of the HESS J1912+101 region does have an energy break at 0.67 ± 0.14 GeV, with photon indices of 0.87 ± 0.08 below the break, and 2.49 ± 0.11 above the break.

Table 1
Spatial Models Tested for the Gigaelectronvolt γ-Ray Emission Above 2 GeV

Morphology(>2GeV)	TS	TS_{ext}	Best−fit Extension	Ndf[a]	ΔAIC[b]
Model 1 (1 point)	178	⋯	⋯	4	0
Model 2 (2 point)	202	⋯	⋯	8	−16
Model 3 (Disk)	311	133	$R_{68} = 0.515^{\circ}{}^{+0.02\circ}_{-0.03\circ}$	5	−131
Model 4 (Gaussian)	318	139	$R_{68} = 0.697^{\circ}{}^{+0.05\circ}_{-0.04\circ}$	5	−138
Model 5 (Disk+point)	316	⋯	⋯	9	−128
Model 6 (Gaussian+point)	321	⋯	⋯	9	−133
Model 7 (Two half-disks)	325	147	⋯	7	−141
Model 8 (H. E. S. S. map)	267	89	$R_{\rm in(out)} = 0.^{\circ}32(0.^{\circ}49)$[c]	2	−93

Notes.
[a] Degrees of freedom.
[b] Calculated with respect to Model 1.
[c] Best-fit radius from HESS ring template (Abdalla et al. 2018).

Table 2
Comparison of Spectral Indices for a PL between 2 GeV and 1 TeV with Two Half-disks

Spatial Model	Index	Photon Flux (10^{-9} ph cm^{-2} s^{-1})
Whole disk	2.37 ± 0.08	2.96 ± 0.19
SrcN	2.21 ± 0.04	1.59 ± 0.10
SrcS	2.68 ± 0.09	1.46 ± 0.11

In order to obtain the spectral energy distributions (SEDs) of both sources, we divided the data in the 100 MeV to 1 TeV energy range into 12 logarithmically equal intervals and performed the same likelihood fitting analysis for each interval. The flux normalizations of all sources are left free, while the spectral indices are fixed. For the interval with a TS value less than 5.0, the upper limit is calculated at the 95% confidence level using a Bayesian method (Helene 1983). The resulting SEDs of the whole disk and SrcN/S are shown in Figure 3, together with the best-fit global PL/BPL spectra in the energy range of 100 MeV to 1 TeV. We also searched for spectral differences between the northern and southern regions of HESS J1912+101, and the spectra data points are listed in Table 4. We find that the spectrum of the southern part also shows a break near $E_b \sim 0.7$ GeV, while a single PL is adequate to describe the gigaelectronvolt emission for the northern part.

3. CO Observations

The vibration rotation CO emission lines are commonly used tracers for molecular material. We make use of the ^{13}CO($J = 1$–0) data from the Boston University-FCRAO Galactic Ring Survey project to trace MoCs, using the SEQUOIA multi-pixel array receiver on the FCRAO 14 m telescope. The GRS possesses excellent sensitivity (<0.4 K), high spectral resolution (0.2 km s^{-1}), angular resolution (46″), and sampling (22″). The detailed observing strategy, the instrument, and the quality of the CO observations can be found in Jackson et al. (2006). In this section, We inspect the ^{13}CO line profiles of the MoCs toward this region to search for kinematic evidence for gas distribution due to external interaction (Frail & Mitchell 1998; Reach et al. 2005; Jiang et al. 2010; Kilpatrick et al. 2016). The work of Su et al. (2017) combined with the H I self-absorption method of Roman-Duval et al. (2009) suggests that the giant molecular gas complex at a velocity of $V_{\rm LSR} \sim +60$ km s^{-1} (Aharonian et al. 2008b; Su et al. 2017) is associated with an old teraelectronvolt SNR candidate (Puehlhofer et al. 2015; Gottschall et al. 2017) near the kinematic distance $d_{\rm near} = 4.1$ kpc, which leads to a physical radius of 29.0 pc for the age of $\sim(0.7$–$2) \times 10^5$ yr.

As shown in Figure 4, there is good spatial correspondence between the gas distribution and the intensity of γ-ray emission. Particularly, the γ-ray emission coincides well with a dense region of clump A should be the main contributor to SrcS. In order to evaluate the column density of H_2 in this region, a conversion factor of $X_{\rm CO} = 2 \times 10^{20}$ cm^{-2} K^{-1} km^{-1} s is used (Dame et al. 2001; Bolatto et al. 2013), and $N_{\rm H_2}$ can be derived as $N_{\rm H_2} = X_{\rm CO} \times W_{\rm CO}$. Thus, the mass of the molecular complex can be calculated from $W_{\rm CO}$ as

$$M = \frac{m_{\rm H}}{X} D^2 \Delta\Omega_{\rm px} X_{\rm CO} \sum_{\rm px} W_{\rm CO} \propto N_{\rm H_2}, \quad (1)$$

where X is the H mass fraction, which is equal to $1/2.8$ if a relative helium abundance of 25% is assumed, $m_{\rm H}$ is the mass of the H nucleon, $N_{\rm H} = 2N_{\rm H_2}$ represents the sum column density of the hydrogen atom in each pixel, and $\Delta\Omega_{\rm px}$ corresponds to the solid angle subtended for each pixel in the map. The term $\sum_{\rm px} W_{\rm CO}$ takes into account the binning in the velocity of the data cube and is obtained by summing the map content for the pixels in the desired sky region and desired velocity range and scaled by the bin size in velocity.

By using the estimation made for $N_{\rm H_2}$ we obtain the mass of the molecular cloud through the relation, the total mass of gas within $0.^{\circ}1$ of clump A is estimated to be about $M_A = 4.3 \times 10^4\, d_{4.1}^2\, M_\odot$. Assuming a spherical geometry of the gas distribution, we estimate the volume to be $V_A = \frac{4\pi}{3} R^3$, where $R = {\rm d} \times \theta$, the average H_2 cubic density in this region is about $n_A = 1140 {\rm d}_{4.1}^{-1}$ cm^{-3}. For clump B, assuming the CO distribution in projection with the ellipse, the mass of gas within clump B is estimated to be about $M_{\rm B} = 1.6 \times 10^5\, d_{4.1}^2\, M_\odot$. Considering the volume $V_{\rm B} = \frac{4\pi}{3} R1R2^2$ (R1 = $0.^{\circ}25$ and $R2 = 0.^{\circ}15$, respectively), the average H_2 cubic density is about $n_B = 755 {\rm d}_{4.1}^{-1}$ cm^{-3}. For the whole disk region, the total mass of gas within $0.^{\circ}515$ is estimated to be $M_{\rm Disk} = 5.6 \times 10^5\, d_{4.1}^2\, M_\odot$, average density is approximately $n_{\rm Disk} = 110 {\rm d}_{4.1}^{-1}$ cm^{-3}, which is consistent with the measurements from Sun et al. (2022), and the density of

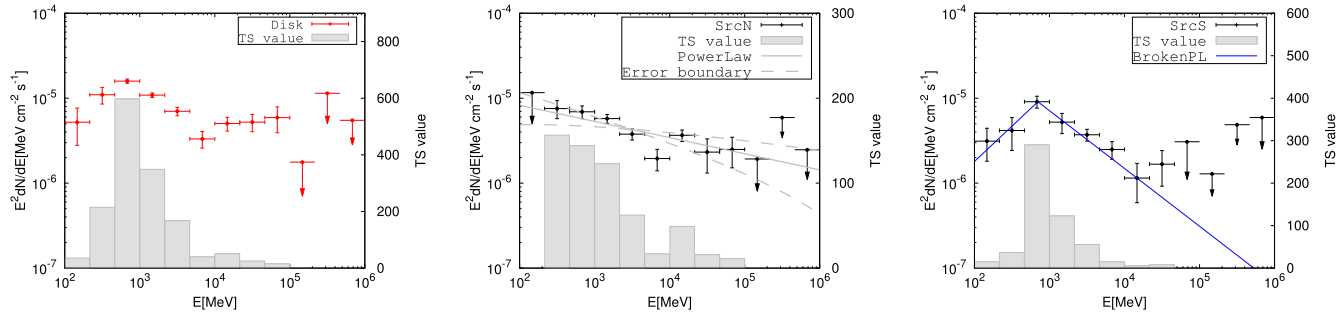

Figure 3. SED of the whole disk (left panel), SrcN (middle panel), and SrcS (right panel) as measured by Fermi-LAT in the energy range of 0.1–1000 GeV. When the TS value of the data point is less than 5, an upper limit is calculated at the 95% confidence level using a Bayesian method denoted by arrows. The gray histogram denotes the TS value for each bin. For SrcN, a single PL is able to fit the Fermi-LAT data points with the gray solid line, and the gray dash lines show the Fermi 68% confidence band. For SrcS, the best-fit BPL spectrum is shown as the blue solid line.

Table 3
Spectral Fit Parameters between 0.1 and 1000 GeV

Spatial Model	Spectral Type	$\Gamma 1$	$\Gamma 2$	E_b(MeV)	Photon Flux (10^{-8} photon cm^{-2} s^{-1})	TS
Whole disk	PL	2.25 ± 0.12	⋯	⋯	11.2 ± 0.05	1342
	BPL	0.87 ± 0.08	2.49 ± 0.11	673 ± 145	9.88 ± 0.04	1547
SrcN	PL	2.19 ± 0.12	⋯	⋯	4.94 ± 0.03	591
SrcS	PL	2.55 ± 0.08	⋯	⋯	5.78 ± 0.04	625
	BPL	0.45 ± 0.05	2.72 ± 0.08	686 ± 133	5.96 ± 0.03	644

Table 4
Fermi-LAT Spectral Data Points of the HESS J1912+101 Region

Energy Band (MeV)	Photon Flux of the Whole Disk (ph cm^{-2} s^{-1})	TS Value of the Whole Disk	Photon Flux of the Northern Region (ph cm^{-2} s^{-1})	TS Value of the Northern Region	Photon Flux of the Southern Region (ph cm^{-2} s^{-1})	TS Value of the Southern Region
100–215	$(2.79 \pm 1.3) \times 10^{-8}$	35	6.21×10^{-8}	<5.0	$(1.31 \pm 0.7) \times 10^{-8}$	25
215–464	$(2.74 \pm 0.61) \times 10^{-8}$	215	$(1.88 \pm 0.45) \times 10^{-8}$	157	$(1.04 \pm 0.43) \times 10^{-8}$	37
464–10^3	$(1.84 \pm 0.11) \times 10^{-8}$	597	$(8.02 \pm 1.36) \times 10^{-9}$	144	$(1.05 \pm 0.17) \times 10^{-8}$	290
10^3–2.15×10^3	$(5.82 \pm 0.35) \times 10^{-9}$	349	$(3.08 \pm 0.37) \times 10^{-9}$	92	$(2.81 \pm 0.75) \times 10^{-9}$	123
2.15×10^3–4.64×10^3	$(1.74 \pm 0.20) \times 10^{-9}$	168	$(9.42 \pm 1.38) \times 10^{-10}$	82	$(9.24 \pm 0.15) \times 10^{-10}$	106
4.64×10^3–10^4	$(3.83 \pm 0.85) \times 10^{-10}$	40	$(2.25 \pm 0.64) \times 10^{-10}$	17	$(2.88 \pm 0.67) \times 10^{-10}$	25
10^4–2.15×10^4	$(2.70 \pm 0.49) \times 10^{-10}$	51	$(1.96 \pm 0.30) \times 10^{-10}$	49	$(6.15 \pm 2.99) \times 10^{-11}$	5
2.15×10^4–4.64×10^4	$(1.32 \pm 0.31) \times 10^{-10}$	25	$(5.77 \pm 2.52) \times 10^{-11}$	16	$(4.16 \pm 1.86) \times 10^{-11}$	8
4.64×10^4–10^5	$(6.82 \pm 2.30) \times 10^{-11}$	15	$(2.88 \pm 1.13) \times 10^{-11}$	11	3.54×10^{-11}	<5.0
10^5–2.15×10^5	9.45×10^{-12}	<5.0	1.03×10^{-11}	<5.0	6.89×10^{-12}	<5.0
2.15×10^5–4.64×10^5	2.84×10^{-11}	<5.0	1.47×10^{-11}	<5.0	1.21×10^{-11}	<5.0
4.64×10^5–10^6	6.33×10^{-12}	<5.0	2.85×10^{-12}	<5.0	6.83×10^{-12}	<5.0

Note. The upper limits at the 95% confidence level are calculated for energy bins with TS values smaller than 5.0.

clumps A/B is in accord with the results measured by Su et al. (2017).

4. Discussion

The multi-band observations show the composition of this area is very complex. In the X-ray band, Chang et al. (2008) analyzed Chandra data but no convincing X-ray counterpart was detected. In the radio band, results from NRAO/VLA at 1.4 GHz (Condon et al. 1998) and MAGPIS (Helfand et al. 2006) show no obvious counterpart to the teraelectronvolt source. A recent study by Reich & Sun (2019) found possible excessive polarized radio emission at a partial shell, but the strong background from the Galactic plane makes it difficult to measure the flux from this source. In the γ-ray energy band, Sun et al. (2022) propose a young massive star cluster scenario, where CRs may be accelerated by the interaction of YMC Mc20 with surrounding gas; however, given the obvious deviation in location as shown in Figure 2, there is little evidence of an association between gigaelectronvolt emission and Mc20. Zhang et al. (2020) show that a PWN scenario is also possible even without radio and X-ray detection of the PWN, while with the enlargement of the data volume and the detailed spectral analysis in the megaelectronvolt to gigaelectronvolt energy band, the PWN scenario has difficulty fulfilling all conditions to interpret the soft spectral components below 10 GeV, especially the prominent energy break around several hundred megaelectronvolts. Zeng et al. (2021) shows that the

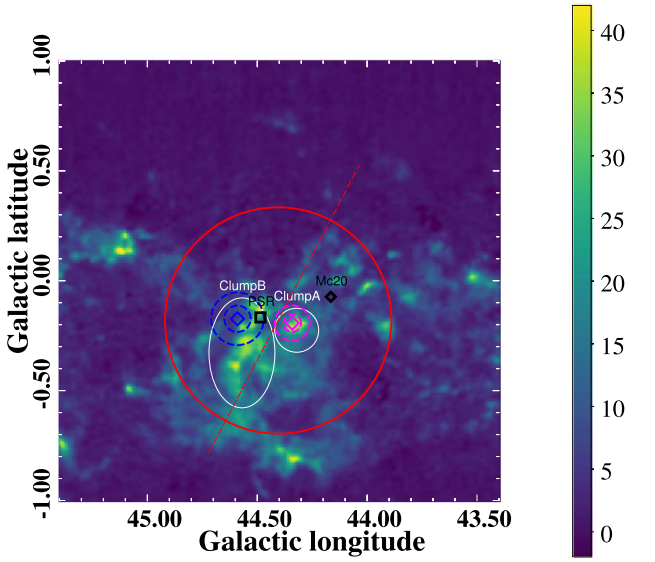

Figure 4. Integrated ^{13}CO ($J = 1$–0) emission intensity (K km s^{-1}) toward HESS J1912+101 at 110.201 GHz in the velocity range of 58.5–62.0 km s^{-1} (BU-FCRAO Galactic Ring Survey data; Jackson et al. 2006). The red circle shows the size of the best-fit whole-disk template, the same as in Figure 2. The white ellipse corresponds to molecular clump B and the white circle corresponds to molecular clump A, which are coincident with the position of the highest γ-ray excesses marked by blue and magenta diamonds. The dashed circles are the same as in Figure 2, respectively.

old age of the SNR rules out a leptonic origin for the teraelectronvolt emission and the more extended diffuse gigaelectronvolt emission should come from SNR interacting with molecular clouds (Su et al. 2017).

The Fermi-LAT data analysis above shows significantly energy-dependent morphology in the region around HESS J1912+101. The γ-ray emission in the south lobe has a soft spectrum with an index of ∼2.7 above 2 GeV, and there is a good spatial correspondence between the γ-ray excess and molecular cloud clump A. For the north lobe, the soft gigaelectronvolt spectrum with an index of ∼2.2 makes it very incompatible with the typical γ-ray PWNe, such as HESS J1640-465 (Xin et al. 2018) and HESS J1825-137 (Principe et al. 2020); meanwhile, the flux from the direction of 4FGL J1913.3+1019 is more than one order of magnitude lower (Zeng et al. 2021) than the northern lobe, combined with no γ-ray excess measured around the location of pulsar PSR J1913 +101 and the lack of radio/X-ray counterparts also disfavor the leptonic scenario. Like W28 and W44, SrcN/S can be interpreted as arising from escaping CRs interacting with surrounding molecular clouds with most of them projected within the teraelectronvolt shell of the SNR.

To explain the γ-ray emission from the whole-disk region, SrcN, and SrcS, respectively, we assume an instantaneous injection of protons into a uniform emission zone disk/N/S at $T = 100$ kyr ago. The injected proton spectrum is adopted to be a BPL spectrum:

$$Q(E) = Q_0 \frac{(E/E_{p,\mathrm{br}})^{-\gamma_1}}{1 + (E/E_{p,\mathrm{br}})^{\gamma_2-\gamma_1}}. \quad (2)$$

Here γ_1 and γ_2 are the low- and high-energy spectral indices, respectively. $E_{p,\mathrm{br}}$ represents the break energy. Some of the injected protons will be trapped in the SNR while others can escape via diffusion. Considering the hard γ-ray spectrum above 10 GeV, we have $\gamma_1 = 2.1$ and $\gamma_2 = \gamma_1 + 1$. And the break energy of protons is set to be $E_{p,\mathrm{br}} = 40$ TeV. The distribution of the escaped protons is given by Thoudam & Hörandel (2012), Liu et al. (2020), and Li et al. (2023) a

$$N_p(E, r_s, T) = \frac{Q(E)}{[4\pi D(E)T]^{\frac{3}{2}}} \exp\left[\frac{-r_s^2}{4D(E)T}\right]. \quad (3)$$

Here, the diffusion coefficient is assumed to be uniform and taken to be $D(E) = \chi D_0 (E/E_0)^\delta$ for $E > E_0$, where $D_0 = 1 \times 10^{28}$ cm^2 s^{-1} at $E_0 = 10$ GeV and $\delta = 1$. Under the assumption that the distance is 4.1 kpc, the source radius is calculated to be $r_s = 37$ pc, which correspond to 0.°515. While the actual distance between the two γ-ray excesses in the northern/southern lobe and SNR shell cannot be constrained by observations due to projection effects, we adopted r_s as the distance between the injection site and the emitting molecular clouds in the following model building part. For an injected source spectrum given by $Q(E) \propto E^{-\Gamma}$ and $D(E) \propto E^\delta$, Equation (3) shows that at high energies, $N_p(E)$ will follow $N_p(E) \propto E^{-\left(\Gamma+\frac{3}{2}\delta\right)}$ with a low energy spectral cutoff at E_b with $\sqrt{4D(E_b)T} \simeq r_s$.

In our model, the total energy of injected protons is assumed to be $W_{\mathrm{inj}} = \eta E_{\mathrm{SN}}$, where E_{SN} is the kinetic energy of the SNR with a typical value of 10^{51} erg and the fraction η of the kinetic energy converted into accelerated protons with a typical value of 0.1. The correction factor χ of the diffusion coefficient is a free parameter adjusted to reproduce the observed Fermi spectra. The corresponding γ-ray fluxes are calculated using the *naima* package (Zabalza 2015) with

$$\frac{dN_\gamma}{dE_\gamma} = \frac{M_i c}{4\pi d^2} \int \frac{d\sigma_{pp}}{dE_\gamma}(E_\gamma, E) N_{\mathrm{p}}(E, r) dE, \quad (4)$$

where the differential proton-proton inelastic cross section for γ-ray production, $d\sigma_{pp}/dE_\gamma$, is adopted from Kafexhiu et al. (2014). M_i represents for the total gas mass in different emission zones (i = A, B, disk) and are the same as those given in Section 3.

For the whole-disk region, the resulting γ-ray flux with the parameters $\chi = 0.1$ could explain the observational data for $T = 100$ kyr as indicated by the solid red line in the left panel of Figure 5. And the total energy of escaped protons above 1 GeV in the whole-disk emission zone is calculated to be $W_{\mathrm{escaped,Disk}} = 8.07 \times 10^{48}\ (M_{\mathrm{Disk}}/5.6 \times 10^5\ M_\odot)^{-1}$ erg, while the total energy of trapped protons above 1 GeV in the whole-disk emission zone is calculated to be $W_{\mathrm{trapped}} = 5.78 \times 10^{48} (n_{\mathrm{Disk}}/110\ \mathrm{cm}^{-3})^{-1}$ erg. We note that the diffusion coefficient is one order of magnitude lower than the standard Galactic value, and a larger diffusion coefficient (e.g., $\chi = 1$) would lead to a higher value of $W_{\mathrm{escaped,Disk}}$ to explain the observed flux. The parameter of $\chi = 0.1$ could also explain the γ-ray emission from SrcN(S) with the total energy of protons in the emission region B(A) above 1 GeV is calculated as $W_{\mathrm{escaped,SrcN(S)}} = 1.45(4.29) \times 10^{49}\ (M_{\mathrm{B(A)}}/1.6(4.3) \times 10^{5(4)}\ M_\odot)^{-1}$ erg and the trapped proton energy value is adopted as half of W_{trapped}. The soft gigaelectronvolt spectrum however requires a value of δ as high as 1. The more extended soft gigaelectronvolt emission on the other hand may be attributed to a new component emerging from ongoing shock–cloud interactions (Su et al. 2017;

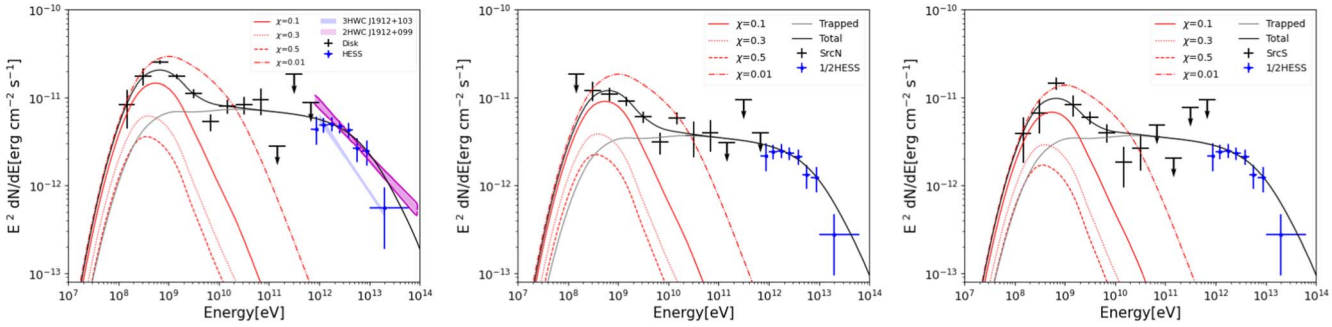

Figure 5. Hadronic modeling of the multiwavelength γ-ray spectra of the whole disk (left), SrcN (middle), and SrcS (right). The solid, dashed, dotted, and dashed–dotted red lines indicate the escaped scenarios with different χ values. The gray solid line in each panel shows the hadronic model for injected protons with a BPL spectrum. The black solid lines show the total contributions from trapped and escaping ions. Blue data points in the left panel show the HESS J1912+101 energy flux spectra extract from Abdalla et al. (2018), and the blue and magenta butterflies show the best-fit PL model from 3HWC J1912+103 (Albert et al. 2020) and 2HWC J1912+099 (Abeysekara et al. 2017), respectively. The teraelectronvolt fluxes from SrcN/S are assumed to be half of the total fluxes.

Liu et al. 2022). Note that the shock–cloud interaction is most evident to the south where the gigaelectronvolt shell extends well beyond the teraelectronvolt shell (Figure 1).

5. Conclusions

We analyzed the megaelectronvolt to gigaelectronvolt γ-ray emission in the vicinity of HESS J1912+101 using 14 yr of Fermi-LAT data and found that the overall γ-ray spectrum of HESS J1912+101 exhibits a break near 0.7 GeV with a significance of $\sim 14.3\sigma$. The photon indices below and above the energy break are 0.87 ± 0.08 and 2.49 ± 0.11, respectively. There is also evidence of spectral hardening above 10 GeV. Furthermore, we found that the gigaelectronvolt emission is more extended than the teraelectronvolt emission, confirming an earlier result (Zeng et al. 2021), and the morphology of the γ-ray emission varies with energy. The spectra of the northern and southern half-disks are very different. The spectrum from the SrcS has a break energy similar to that of the whole region, while the spectrum from the SrcN can be described well by a single PL with an index of 2.19 ± 0.12. The SrcN also dominates the flux above 10 GeV. Such kind of spectral variations was also found in SNR Puppis A (Xin et al. 2017), implying a softer spectrum of accelerated particles in a higher density environment.

We found two clumps of very dense gases in this region, whose velocity range of 58.5–62.0 km s^{-1} is consistent with the distance estimation for HESS J1912+101, and molecular clouds were detected throughout the region. We fit the γ-ray SEDs using an escape model in the hadronic scenario for the γ-ray emission, which attributes the hard high-energy spectrum to ions still trapped in the SNR, and the low energy emission to escaping ions. The diffusion coefficient in the escaping zone needs to be proportional to the energy to fit the spectrum near 1 GeV. Considering the good spatial correspondence between molecular clouds and gigaelectronvolt emission, especially in the southern part, we suggest that although the spectra can be fitted with the escape model, the soft gigaelectronvolt spectrum of the southern source favors a new soft component emerging from shock–cloud interactions. Therefore, the more extended gigaelectronvolt emission may also be attributed to a soft component emerging from ongoing shock–cloud interactions, which reduce the shock speed significantly (Liu et al. 2022). Such a soft component may also emerge as CRs propagate via a dense magnetized molecular cloud with some CR scattering waves dampened via ion-neutral coupling (Malkov et al. 2011). On the other hand, given the high spin-down luminosity of PSR J1913+1011 (Morris et al. 2002) and the presence of a star cluster (Sun et al. 2022), the extended source studied here may have contributions from them as well (Duvidovich & Petriella 2023). Further observations are required to distinguish these scenarios.

Acknowledgments

We thank Haiming Zhang, Ruoyu Liu, Yang Su, L.D. Anderson, and P.P. Delia for invaluable discussions. This work makes use of molecular line data from the Boston University-FCRAO Galactic Ring Survey (GRS). This work is supported by the National Natural Science Foundation of China under grant Nos. U1931204, 12103040, and 12147208, the Natural Science Foundation for Young Scholars of Sichuan Province, China (No. 2022NSFSC1808), and the Fundamental Research Funds for the Central Universities (No. 2682022ZTPY013).

ORCID iDs

Yuan Li https://orcid.org/0009-0003-4873-6770
Siming Liu https://orcid.org/0000-0003-1039-9521
Yu He https://orcid.org/0000-0002-2745-9001

References

Abdalla, H., Abramowski, A., (H. E. S. S. Collaboration), et al. 2018, A&A, 612, A8
Abdo, A. A., Ackermann, M., Ajello, M., et al. 2009, ApJL, 706, L1
Abdo, A. A., Ackermann, M., Ajello, M., et al. 2010, ApJ, 712, 459
Abdollahi, S., Acero, F., Ackermann, M., et al. 2020, ApJS, 247, 33
Abeysekara, A. U., Albert, A., Alfaro, R., et al. 2017, ApJ, 843, 40
Acciari, V. A., Ansoldi, S., (MAGIC Collaboration), et al. 2023, A&A, 670, A8
Ackermann, M., Ajello, M., Allafort, A., et al. 2013, Sci, 339, 807
Aharonian, F., Akhperjanian, A. G., Bazer-Bachi, A. R., et al. 2008a, A&A, 481, 401
Aharonian, F., Akhperjanian, A. G., Barres de Almeida, U., et al. 2008b, A&A, 484, 435
Aharonian, F. A., Akhperjanian, A. G., Aye, K. M., et al. 2004, Natur, 432, 75
Aharonian, F. A., & Atoyan, A. M. 1996, A&A, 309, 917
Akaike, H. 1974, ITAC, 19, 716
Albert, A., Alfaro, R., Alvarez, C., et al. 2020, ApJ, 905, 76
Atwood, W. B., Abdo, A. A., Ackermann, M., et al. 2009, ApJ, 697, 1071
Bolatto, A. D., Wolfire, M., & Leroy, A. K. 2013, ARA&A, 51, 207
Chang, C., Konopelko, A., & Cui, W. 2008, ApJ, 682, 1177
Condon, J. J., Cotton, W. D., Greisen, E. W., et al. 1998, AJ, 115, 1693
Dame, T. M., Hartmann, D., & Thaddeus, P. 2001, ApJ, 547, 792
Duvidovich, L., & Petriella, A. 2023, A&A, 672, A195
Frail, D. A., & Mitchell, G. F. 1998, ApJ, 508, 690

Gabici, S., Aharonian, F. A., & Casanova, S. 2009, MNRAS, 396, 1629
Ginzburg, V. L., & Syrovatskii, S. I. 1964, The Origin of Cosmic Rays (New York: Macmillan)
Gottschall, D., Capasso, M., Deil, C., et al. 2017, AIP Conf. Ser. 1792, 6th Int. Symp. on High Energy Gamma-Ray Astronomy (Melville, NY: AIP), 040030
Hanabata, Y., Katagiri, H., Hewitt, J. W., et al. 2014, ApJ, 786, 145
Helene, O. 1983, NIMPR, 212, 319
Helfand, D. J., Becker, R. H., White, R. L., Fallon, A., & Tuttle, S. 2006, AJ, 131, 2525
Hillas, A. M. 2005, JPhG, 31, R95
Jackson, J. M., Rathborne, J. M., Shah, R. Y., et al. 2006, ApJS, 163, 145
Jiang, B., Chen, Y., Wang, J., et al. 2010, ApJ, 712, 1147
Kafexhiu, E., Aharonian, F., Taylor, A. M., & Vila, G. S. 2014, PhRvD, 90, 123014
Kilpatrick, C. D., Bieging, J. H., & Rieke, G. H. 2016, ApJ, 816, 1
Lande, J., Ackermann, M., Allafort, A., et al. 2012, ApJ, 756, 5
Li, H., & Chen, Y. 2010, MNRAS Lett., 409, L35
Li, Y., Xin, Y., Liu, S., & He, Y. 2023, ApJ, 945, 21
Liu, S., Zeng, H., Xin, Y., & Zhu, H. 2020, ApJL, 897, L34
Liu, S., Zeng, H., Xin, Y., & Zhang, Y. 2022, RvMPP, 6, 19
Malkov, M., & Drury, L. O. 2001, RPPh, 64, 429
Malkov, M. A., Diamond, P. H., & Sagdeev, R. Z. 2011, NatCo, 2, 194
Mattox, J. R., Bertsch, D. L., Chiang, J., et al. 1996, ApJ, 461, 396
Messineo, M., Davies, B., Ivanov, V. D., et al. 2009, ApJ, 697, 701
Morris, D. J., Hobbs, G., Lyne, A. G., et al. 2002, MNRAS, 335, 275
Ohira, Y., Murase, K., & Yamazaki, R. 2011, MNRAS, 410, 1577
Peron, G., Aharonian, F., Casanova, S., Zanin, R., & Romoli, C. 2020, ApJL, 896, L23
Principe, G., Mitchell, A. M. W., Caroff, S., et al. 2020, A&A, 640, A76
Puehlhofer, G., Brun, F., Capasso, M., et al. 2015, ICRC, 34, 1039
Reach, W. T., Rho, J., & Jarrett, T. H. 2005, ApJ, 618, 297
Reich, W., & Sun, X.-H. 2019, RAA, 19, 045
Rodriguez Marrero, A. Y., Torres, D. F., de Cea del Pozo, E., Reimer, O., & Cillis, A. N. 2008, ApJ, 689, 213
Roman-Duval, J., Jackson, J. M., Heyer, M., et al. 2009, ApJ, 699, 1153
Su, Y., Zhou, X., Yang, J., et al. 2017, ApJ, 845, 48
Sun, X.-N., Yang, R.-Z., & Liang, E.-W. 2022, A&A, 659, A83
Thoudam, S., & Hörandel, J. R. 2012, MNRAS, 419, 624
Uchiyama, Y., Funk, S., Katagiri, H., et al. 2012, ApJL, 749, L35
Wood, M., Caputo, R., Charles, E., et al. 2017, ICRC, 35, 824
Xin, Y.-L., Guo, X.-L., Liao, N.-H., et al. 2017, ApJ, 843, 90
Xin, Y.-L., Liao, N.-H., Guo, X.-L., et al. 2018, ApJ, 867, 55
Zabalza, V. 2015, ICRC, 34, 922
Zeng, H., Xin, Y., Zhang, S., & Liu, S. 2021, ApJ, 910, 78
Zhang, H.-M., Xi, S.-Q., Liu, R.-Y., et al. 2020, ApJ, 889, 12